

# GYSELA , a full- $f$ global gyrokinetic Semi-Lagrangian code for ITG turbulence simulations

V. Grandgirard, Y. Sarazin, X. Garbet, G. Dif-Pradalier, Ph. Ghendrih\*, N. Crouseilles, G. Latu, E. Sonnendrücker<sup>†</sup> and N. Besse, P. Bertrand\*\*

\*Association Euratom-CEA, CEA/DSM/DRFC CEA-Cadarache, France.

<sup>†</sup>IRMA, Université Louis Pasteur, 7, rue René Descartes, 67084 Strasbourg Cedex, France.

\*\*LPMIA, Université Henri Poincaré-Nancy 1, BP 239, 54506 Vandoeuvre-les-Nancy, France

**Abstract.** This work addresses non-linear global gyrokinetic simulations of ion temperature gradient (ITG) driven turbulence with the GYSELA code. The particularity of GYSELA code is to use a fixed grid with a Semi-Lagrangian (SL) scheme and this for the entire distribution function. The 4D non-linear drift-kinetic version of the code already shows the interest of such a SL method which exhibits good properties of energy conservation in non-linear regime as well as an accurate description of fine spatial scales. The code has been upgraded to run 5D simulations of toroidal ITG turbulence. Linear benchmarks and non-linear first results prove that semi-lagrangian codes can be a credible alternative for gyrokinetic simulations.

**Keywords:** Turbulence, Gyrokinetic, Vlasov equation, Semi-Lagrangian scheme

## INTRODUCTION

Non-linear gyrokinetic simulations are playing an increasingly important role in understanding anomalous transport in magnetically confined fusion plasmas. In spite of considerable progress, the choice of the method for solving the Vlasov equation is still in debate. The most widespread method is the Lagrangian scheme (typically Particle In Cell codes). An another alternative is the Eulerian method. These two approaches have already proved their efficiency. However the fact that the PIC simulations can be affected by numerical noise is still subject to controversy [1]. Techniques of "optimal loading" [2] and filtering have been recently developed to improve this problem. On the other hand, Eulerian codes require numerical schemes of high order to limit numerical dissipation. This paper deals with gyrokinetic simulations performed with a new method based on a semi-Lagrangian (SL) scheme [3]. In the GYSELA code the full distribution function is evolved on a fixed grid in the phase space, moving backwards in time along the characteristics. A 4D drift-kinetic slab-ITG version of the code has already shown good properties of energy conservation in non-linear regime as well as an accurate description of fine spatial scales [4, 5]. The first results obtained with the new 5D gyrokinetic toroidal version of GYSELA are presented. The remainder of this paper is organized as follows. The gyrokinetic toroidal 5D model is described, in section 2. The section 3 is focused on the numerical methods used in GYSELA and more specifically the semi-lagrangian scheme. Benchmarks with the classical CYCLONE linear testbed and the so-called Rosenbluth-Hinton test are presented in section 4 while the first non-linear

results are developed in section 5. Finally, a summary is given in section 6.

## A GYROKINETIC 5D MODEL IN TOROIDAL GEOMETRY

### Physical model

The model focuses on the turbulent transport driven by the collisionless ITG instability in a simple toroidal geometry (the magnetic flux surfaces are taken to be concentric torii with circular poloidal cross-sections). Since the turbulence frequency  $\omega$  is much smaller than the ion cyclotron frequency  $\omega_c = \frac{e_i B_0}{m_i}$  ( $e_i = Z_i e$  is the ion charge and  $m_i$  the ion mass), the gyrokinetic description is appropriate. The magnetic configuration is a circular concentric tokamak configuration:  $\vec{B} = \frac{B_0 R_0}{R} \vec{b}$  with the unit vector  $\vec{b} = \left(1/\sqrt{1+(r/qR)^2}\right) (\vec{e}_\varphi + r/(qR)\vec{e}_\theta)$ .  $B_0$  and  $R_0$  correspond to the magnetic field and the major radius of the torus computed at the magnetic axis, with  $R = R_0 + r \cos \theta$ .  $\vec{e}_\theta$  and  $\vec{e}_\varphi$  are the unit vectors in the two periodic directions, poloidal and toroidal respectively. The safety factor profile  $q(r) = \vec{B} \cdot \vec{\nabla} \phi / \vec{B} \cdot \vec{\nabla} \theta$  is defined by the three parameters  $q_0$ ,  $\delta_q$ , and  $\alpha_q$  such that  $q(r) = q_0 + \delta_q (r/a)^{\alpha_q}$ . The fluctuations of the magnetic field are neglected. Thus the electrostatic approximation is used to compute the electric field, i.e.  $\vec{E} = -\vec{\nabla} \phi$ , where the scalar  $\phi$  represents the electric potential. Electrons are assumed adiabatic, so that  $\delta n_e/n_0 = e(\phi - \langle \phi \rangle)/T_e$ , where  $n_0$  is the equilibrium particle density profile. The brackets  $\langle \cdot \rangle$  refer to the magnetic flux surface average:  $\langle \cdot \rangle = \iint \cdot d\theta d\varphi / (2\pi)^2$ . Taking into account the velocity drifts up to the first order in  $\omega/\omega_c \ll 1$  and in the limit  $\varepsilon = r/R \ll 1$ , the trajectories of the ion guiding-centers are governed by:

$$\frac{dr}{dt} = v_{\bar{E}r} + v_{gr} \quad ; \quad \frac{d\theta}{dt} = \frac{v_{\parallel}}{q(r)R} + \frac{1}{r} (v_{\bar{E}\theta} + v_{g\theta}) \quad ; \quad \frac{d\varphi}{dt} = \frac{v_{\parallel}}{R} \quad (1)$$

$$\frac{dv_{\parallel}}{dt} = -\frac{e_i}{m_i} \nabla_{\parallel} \bar{\phi} - \frac{\mu}{m_i} \nabla_{\parallel} B + \frac{v_{\parallel}}{B} (\vec{v}_{\bar{E}} \cdot \vec{\nabla} B) \quad \text{with } \nabla_{\parallel} = \frac{1}{R} \left[ \partial_{\varphi} + \frac{1}{q(r)} \partial_{\theta} \right] \quad (2)$$

$v_{\parallel}$  is the velocity parallel to the magnetic field. In the adiabatic limit, where the characteristic evolution times of the system are much faster than the evolution time of the magnetic field and where the spatial excursion of the particles is small compared to the space-evolution of this field, the magnetic momentum  $\mu = m_i v_{\perp}^2 / (2B)$  is an invariant ( $v_{\perp}$  being the velocity in every plane orthogonal to the magnetic field direction). Therefore this fifth dimension acts as a parameter. The subscripts  $r$  and  $\theta$  refer to the radial and poloidal components, respectively. The electric drift velocity  $v_{\bar{E}}$  is computed with the gyroaverage of the electric potential  $\bar{\phi}$ :  $\vec{v}_{\bar{E}} = (\vec{B} \times \vec{\nabla} \bar{\phi}) / B^2$ . At low  $\beta$ , the curvature drift velocity  $\vec{v}_{g\perp}$  is given by  $\vec{v}_{g\perp} = \left( \frac{\vec{B}}{eB^2} \times \frac{\nabla B}{B} \right) (m_i v_{\parallel}^2 + \mu B)$  which reads, in the large aspect ratio limit,  $\vec{v}_{g\perp} = v_g [\sin \theta \vec{e}_r + \cos \theta \vec{e}_{\theta}]$  with  $v_g = -(m_i v_{\parallel}^2 + \mu B) / (eB_0 R_0)$ .

Within these approximations the system is governed by two equations. The Vlasov equation which is averaged over the cyclotron motion (the gyroaverage), leading to the so-called gyrokinetic equation involving the guiding-center 5D distribution function

$\bar{f}(r, \theta, \varphi, v_{\parallel}, \mu, t)$ :

$$\frac{\partial \bar{f}}{\partial t} + \frac{dr}{dt} \frac{\partial \bar{f}}{\partial r} + \frac{d\theta}{dt} \frac{\partial \bar{f}}{\partial \theta} + \frac{d\varphi}{dt} \frac{\partial \bar{f}}{\partial \varphi} + \frac{dv_{\parallel}}{dt} \frac{\partial \bar{f}}{\partial v_{\parallel}} = 0 \quad (3)$$

The upper bar refers to the gyroaverage operation. This equation ensures that  $\bar{f}$  is constant along the characteristics (2). The electric quasineutrality provides the self-consistency of the problem, coupling the electric potential  $\phi$  to  $\bar{f}$ . Using the notation  $\vec{\nabla}_{\perp} = (\partial_r, \frac{1}{r}\partial_{\theta})$ , it reads:

$$-\frac{1}{n_0(r)} \nabla_{\perp} \cdot \left[ \frac{n_0(r)}{B_0 \omega_c} \nabla_{\perp} \phi \right] + \frac{e}{T_e(r)} [\phi - \langle \phi \rangle] = \frac{1}{n_0(r)} [n_{Gi}(r, \theta, \varphi) - n_{Gi_{eq}}(r, \theta)] \quad (4)$$

The ion guiding-center density  $n_{Gi}$  is given by:

$$n_{Gi}(r, \theta, \varphi) = 2\pi \int B(r, \theta)/m_i d\mu \int dv_{\parallel} J_0(k_{\perp} \rho_c) \cdot \bar{f}(r, \theta, \varphi, v_{\parallel}, \mu) \quad (5)$$

with the Larmor radius  $\rho_c$ . The first term on the left hand side is known as the polarization term. It corresponds to the difference between the guiding-center density and that of particles. The correction term  $n_{Gi_{eq}}$  is equal to:

$$n_{Gi_{eq}}(r, \theta) = 2\pi \int B(r, \theta)/m_i d\mu \int dv_{\parallel} J_0(k_{\perp} \rho_c) \cdot \bar{f}_{eq}(r, \theta, v_{\parallel}, \mu) \quad (6)$$

The Bessel function  $J_0$ , corresponds to the gyro-average operator in the Fourier space.

## Initial and boundary conditions

The radial profiles of the ion and electron temperature (respectively  $T_i(r)$  and  $T_e(r)$ ) as well as the radial density profile  $n_0(r)$ , are fixed in time and deduced by numerical integration of their gradient profiles given by the two parameters  $\kappa$ ,  $\Delta r$ . For instance,

$$d \log T_i(r)/dr = -\kappa_{T_i} \cosh^{-2}((r - r_p)/\Delta r_{T_i}) \quad (7)$$

with  $r_p$  corresponding to the middle of the radial box. The distribution function is periodic along  $\theta$  and  $\varphi$ . Vanishing perturbations are imposed at the boundaries in the non-periodic directions, namely  $r$  and  $v_{\parallel}$ . Initial conditions consist in an equilibrium distribution function  $f_{eq}$  perturbed either by a single Fourier mode  $(m, n)$  ( $m$  and  $n$  being the poloidal and toroidal wave numbers, respectively), or by the sum of all accessible  $(m, n)$  modes. Previously the equilibrium distribution function was chosen equal to the conventional Maxwellian distribution function  $f_M(r, \theta, v_{\parallel}, \mu) = n_0(r) / \left[ (2\pi T_i(r)/m_i)^{\frac{3}{2}} \right] \exp(-E/T_i(r))$  with  $E = \frac{1}{2} m_i v_{\parallel}^2 + \mu B(r, \theta)$  the energy of the system. But it appears that it is crucial to choose  $f_{eq}$  as function of the motion invariants especially for studying zonal flows. Indeed, breaking this rule leads to the development

of large scale steady flows, which prevent the onset of turbulence (see following non-linear results), consistently with previous observations [6, 7]. The first motion invariant of the system is the energy. The second is the toroidal kinetic momentum  $P_\varphi$  due to the axisymmetric magnetic topology ;  $P_\varphi = e_i \Psi + m_i R v_\varphi$  with  $\Psi$  being the toroidal magnetic flux. The third motion invariant  $\mu$  is an adiabatic invariant. So the equilibrium distribution function is initialized to the conventional Maxwellian where  $r$  is replaced by a new coordinate  $\bar{r}$  which depends on the motion invariants only. The invariant  $\bar{r}$  is chosen as close as possible to the geometric radial coordinate, i.e.

$$\bar{r} = r_p - \frac{q_p}{r_p} \left[ \psi(r) - \psi(r_p) \right] - \frac{m q_p}{e B_0 r_p} \left[ R v_\parallel - R_0 \bar{v}_\parallel \right] \quad (8)$$

where  $\psi(r) = -B_0 \int_0^r \frac{r' dr'}{q}$ . The expression of  $\bar{v}_\parallel = \text{sign}(v_\parallel) \sqrt{2/m} \sqrt{E - \mu B_{\max}} H(E - \mu B_{\max})$  has been chosen to minimize poloidal flows (cf. [8]). With this expression the difference between  $\bar{r}$  and  $r$  is of order  $\rho_*$ , where  $\rho_*$  is a characteristic device size parameter given as  $\rho_i/a$  with  $\rho_i$  the ion Larmor radius and  $a$  the minor radius.

## NUMERICAL METHOD

The discretization of the quasi-neutrality equation (4) and the solving of the  $J_0$  operator are performed via a projection in Fourier space along the two periodic directions ( $\theta$  and  $\varphi$ ) whereas finite differences are used in the radial direction. The resulting tridiagonal system is inverted using a LU decomposition. Concerning the gyroaverage operator, the Bessel function is replaced by a Padé approximation:  $J_0(k_\perp \rho_c) \sim 1/[1 + (k_\perp \rho_c)^2/4]$ . This approximation gives the correct limit at vanishing  $k_\perp \rho_c$ , while keeping  $J_0$  finite in the opposite limit  $k_\perp \rho_c \rightarrow \infty$ . Using the equivalence  $i\vec{k}_\perp \leftrightarrow \vec{\nabla}_\perp$ , the gyroaverage operation of any  $g$  function then leads to the following implicit equation  $[1 - (\rho_c^2/4)\nabla_\perp^2] \bar{g}(r, \theta, \varphi) = g(r, \theta, \varphi)$  where we recall that  $\nabla_\perp^2 = \partial^2 r + (1/r^2)\partial^2 \theta$ . Each Fourier mode  $(m, n)$  of  $\bar{g}$  is then solution of the equation  $[1 - (\rho_c^2/4)(\partial^2 r - m^2/r^2)] \bar{g}^{m,n}(r) = g^{m,n}(r)$ .

## Time-splitting

The Vlasov equation (3) is solved by splitting it into the three following advection equations:  $\partial_t \bar{f} + v_{GC} \cdot \vec{\nabla}_\perp \bar{f} = 0$  ;  $\partial_t \bar{f} + v_\parallel \partial_\varphi \bar{f} = 0$  ;  $\partial_t \bar{f} + \hat{v}_\parallel \partial_{v_\parallel} \bar{f} = 0$ . Let  $\hat{r}\hat{\theta}$  denotes the shift operator in  $(r, \theta)$  direction over a time step  $\Delta t$ , associated to the first equation. Similarly,  $\hat{\varphi}$  and  $\hat{v}_\parallel$  denote the shift operators respectively in the  $\varphi$  (second equation) and  $v_\parallel$  directions (third equation). A splitting of Strang [9] is applied to keep a scheme of second order accuracy. Second order accuracy is obtained by imposing a symmetry in the application of the different shifts. In our case the most efficient sequence is  $(\hat{v}_\parallel/2, \hat{\varphi}/2, \hat{r}\hat{\theta}/2, \hat{r}\hat{\theta}/2, \hat{\varphi}/2, \hat{v}_\parallel/2)$  (where factor 1/2 corresponds to a shift over a  $\Delta t/2$ ) because with this sequence the two  $(r, \theta)$  shifts in 2D can be connected. So that the algorithm time step can be summarized by  $(\hat{v}_\parallel/2, \hat{\varphi}/2, \hat{r}\hat{\theta}, \hat{\varphi}/2, \hat{v}_\parallel/2, \hat{Q})$ , where  $\hat{Q}$

denotes symbolically that at this point the quasi-neutrality equation is solved to compute the electric potential and thereby the electric field. The shifts in the  $\varphi$  and  $v_{\parallel}$  directions are straightforward, but the one in the  $(r, \theta)$  direction requires more attention. Indeed, if we consider the action of the  $r\hat{\theta}$  operator between times  $t - \Delta t$  and  $t + \Delta t$ , the value of the electric field  $\vec{E}$  at time  $t$  is required to keep a time scheme of second order. This value is calculated by using a leap-frog method, which involves the use of two distribution functions shifted in time by one time step.

## Semi-Lagrangian scheme

Let  $\vec{\Gamma}$  be a position vector in the phase space such that  $\vec{\Gamma} = (r, \theta, \varphi, v_{\parallel})$  and let  $\vec{\Gamma}_i$  be a position vector which corresponds to a node of the mesh. The semi-lagrangian method is based on the invariance of the distribution function  $\bar{f}$  along its characteristics Eq. (2), since  $\frac{d\bar{f}}{dt}(\vec{\Gamma}(t), t) = 0$  according to the Vlasov equation (3). Therefore the distribution function can be computed at each time step on the same fixed grid, by using  $\bar{f}(\vec{\Gamma}_i(t_n + \Delta t), t_n + \Delta t) = \bar{f}(\vec{\Gamma}(t_n, \vec{\Gamma}_i, t_n + \Delta t), t_n)$  where  $\vec{\Gamma}(t_n, \vec{\Gamma}_i, t_n + \Delta t)$  represents the solution of the characteristic at time step  $t_n$  is equal to  $\vec{\Gamma}_i$  at time  $t_n + \Delta t$ . The method consists first in finding the foot of the characteristic at the time  $t_n$ :  $\vec{\Gamma}(t_n, \vec{\Gamma}_i, t_n + \Delta t)$ . The second step is to compute  $\bar{f}(\vec{\Gamma}(t_n, \vec{\Gamma}_i, t_n + \Delta t), t_n)$  by interpolation, because at this time, the distribution function is known over the whole fixed grid. This sequence of operations can be applied separately on each advection equation appearing in the time-splitting algorithm. The computation of the foot of the characteristic for the 1D equations in the  $\varphi$  and  $v_{\parallel}$  directions is trivial unlike that for the 2D equation in  $(r, \theta)$ . This 2D equation cannot be divided into two 1D equations because  $\partial_r v_{GC_r} \neq 0$  and  $\partial_{\theta} v_{GC_{\theta}} \neq 0$ . The 2D characteristic equation in the  $(r, \theta)$  cross-section is performed in cartesian coordinates to improve the numerical stability close to the axis. So computing the 2D trajectories is equivalent to solve  $d\vec{X}/dt = \vec{v}_X(\vec{X}, \varphi, t)$  This system is solved by using the parabolic assumption developed in [3]. Let  $\vec{X}_{ij}$  be the position of  $\vec{X}(t_n + \Delta t)$  at time  $t_n + \Delta t$ , then there exists a displacement  $\vec{d}_{ij} = (\alpha_{ij}, \beta_{ij})$  tangent to the parabola such that  $\vec{X}(t_n) = \vec{X}_{ij} - \vec{d}_{ij}$  and  $\vec{X}(t_n - \Delta t) = \vec{X}_{ij} - 2\vec{d}_{ij}$ . This displacement  $\vec{d}_{ij}$  can be calculated by solving the implicit equation  $\vec{d}_{ij} = \Delta t \vec{v}_X(\vec{X}_{ij} - \vec{d}_{ij}, t_n)$  This implicit equation is solved by using a Taylor expansion which is equivalent at second order to a Newton algorithm.

We need then to calculate the value of the distribution function at the characteristic feet, which are no longer grid points. So this is performed by using cubic spline interpolation, which is a good compromise between accuracy and numerical cost. For instance in 2D, let  $N_r$  and  $N_{\theta}$  be the number of points respectively in  $r$  and  $\theta$  directions. Then,  $\bar{f}(r, \theta, \varphi_k, v_{\parallel l}, \mu_m)$  is approximated, for all  $\varphi_k, v_{\parallel l}$ , by a 2D tensor product of cubic B-splines:  $g_2(r, \theta) = \sum_{\alpha=-1}^{N_r+1} \sum_{\beta=-1}^{N_{\theta}+1} c_{\alpha, \beta} \Lambda_{\alpha}(r) \Lambda_{\beta}(\theta)$  where  $\Lambda$  are piecewise cubic polynomials which are twice continuously differentiable (cf [10]).

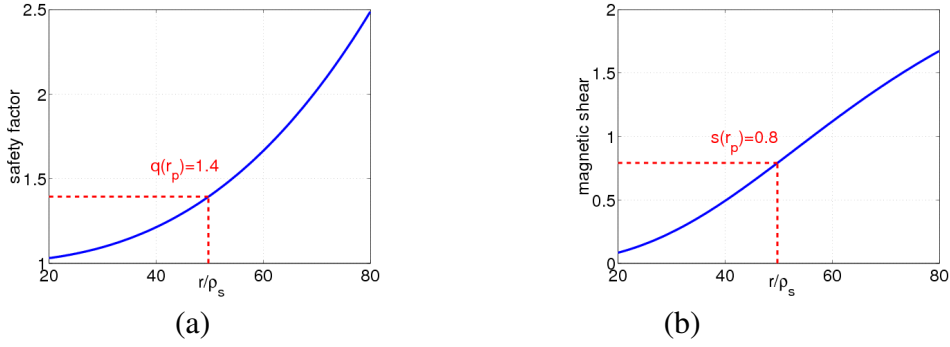


**FIGURE 1.** Radial initial profiles of the safety factor  $q$  such that  $q(r_p) = 1.4$  in (a) and the magnetic shear  $s$  such that  $s(r_p) = 0.8$  in (b).

## LINEAR VALIDATION

### Benchmark with the classical cyclone DIII-D case

The numerical solution is performed using the normalized equations. In our case, the temperature is normalized to  $T_{e0}$ , where  $T_{e0}$  is defined such that  $T_e(r_p)/T_{e0} = 1$ . The time is normalized to the inverse of the ion cyclotron frequency  $\omega_c = e_i B_0 / m_i$ . Velocities, including the parallel velocity, are expressed in units of the ion thermal speed  $v_{T0} = \sqrt{T_{e0}/m_i}$ , the electric potential is normalized to  $T_{e0}/e_i$  and the magnetic field is normalized to  $B_0$ . Therefore by deduction lengths are normalized to the Larmor radius  $\rho_s = m_i v_{T0} / e_i B$  and the magnetic momentum  $\mu$  to  $T_{e0}/B_0$ . In this section, we will show the results of the benchmark test with the cyclone base case [11]. The classical dimensionless parameters are:  $R_0/L_T = 6.92$ ,  $R_0/L_n = 2.2$ ,  $\varepsilon = a/R_0 = 0.18$ ,  $q = 1.4$ ,  $s \equiv (r/q)(dq/dr) = 0.8$ ,  $\rho_* = 1/184.7$  and  $T_e/T_i = 1$ .  $L_T$  and  $L_n$  are the temperature and density gradient scale lengths, respectively. For all the following the simulation domain is limited to the region of  $0.2 < r/a < 0.8$  with fixed boundary conditions. For discretization of the velocity space,  $-4v_{T_i} \leq v_{\parallel} \leq 4v_{T_i}$  and  $0 \leq \mu \leq 7B_0/T_{e0}$  we have used  $(16 \times 8)$  grid points, while  $(128 \times 128 \times 64)$  points have been employed for the  $(r, \theta, \varphi)$  space. The cyclone case is not so simple to perform with a global full- $f$  code as GYSELA. Indeed, these parameters can only be satisfied locally. The initial profiles have been chosen such that the values at the middle of the radial box  $r_p$  are equal to the cyclone values. Therefore the safety factor profile is chosen equal to  $q(r) = 1 + 2.78(r/a)^{2.8}$  to satisfy  $q(r_p) = 1.4$  and  $s(r_p) = 0.8$  (fig. 1). As seen before the density and temperature profiles are initialized by (7) (dashed line on figure 2). But let recall that the equilibrium distribution function is not initialized by the classical Maxwellian but by a function depending on the motion invariants only. Then the gradient profiles which really play a role in the simulation are not  $n_0$  and  $T_i$  but  $n_{eq}(r) = \int J_0 f_{eq} d\theta d_3v$  for the density and  $T_{ieq}(r) = \int J_0 f_{eq} E d\theta d_3v / n_{eq}(r)$  for the temperature. The correction is a correction in  $\rho_*$ . So the effective gradients which really enter in the simulation must be adjusted. In figure 2 the difference is shown for the  $\rho_*$  used to perform the Cyclone test,  $\rho_*$  of  $10^{-2}$ . For this reason the cyclone test has been performed by first

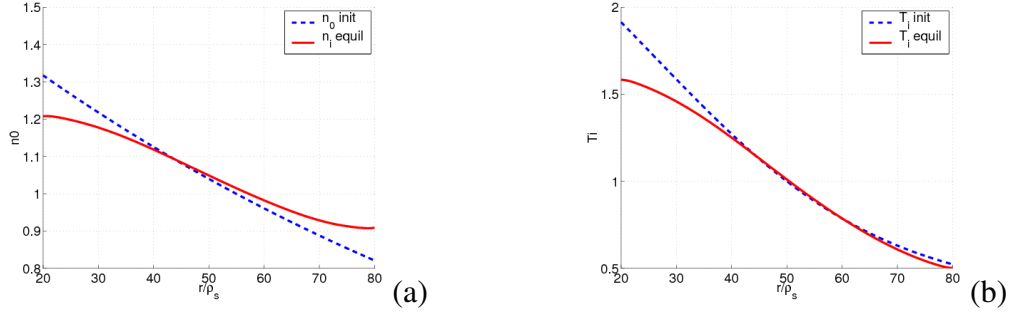


**FIGURE 2.** (a) Comparison between  $n_0(r)$  (dashed line) and  $n_{eq}(r) = \int J_0 f_{eq} d\theta d_3v$  (solid line). (b) Comparison between  $T_i$  (dashed line) and  $T_{ieq}(r) = \int J_0 f_{eq} E d\theta d_3v / n_{eq}(r)$  (solid line).  $n_0$  and  $T_i$  are the initial profiles but the profiles which really play a role in the simulation are the reconstructed profiles  $n_{eq}$  and  $T_{eq}$ .

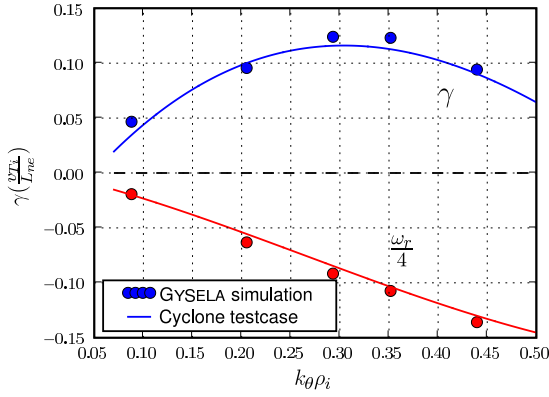


**FIGURE 3.** Linear mode growth rates and frequencies versus  $k_\theta \rho_i$  for the Cyclone DIII-D base case. The GYSELA results are plotted with circle points. The solid line represents a linear interpolation of all the results presented in paper [11].

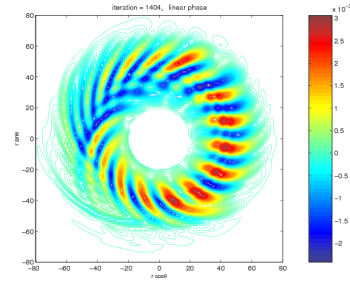


**FIGURE 4.** Poloidal cross-section of the electric potential for the most unstable mode  $(m, n) = (10, -14)$

calibrating the required gradients to recover the growth rate and the frequency of the most unstable mode  $(m, n) = (10, -14)$  (see its ballooning mode structure in figure 4). The corresponding parameters are the following  $\kappa_n = 2.2$ ,  $\Delta_{r_n} = 5$ ,  $\kappa_T = 6.78$ ,  $\Delta_{r_T} = 0.8$ . Then the same parameters have been used to perform the four others simulations for  $(m, n) = (4, -3)$ ,  $(7, -10)$ ,  $(12, -17)$  and  $(21, -15)$ . The results reported on figure 3 show that GYSELA results are in agreement with the results obtained by the other codes.

## Collisionless damping of zonal flow and GAM

Rosenbluth and Hinton [12] have shown that linear collisionless processes do not fully damp poloidal flows driven by ITG. The residual level of the zonal flow after

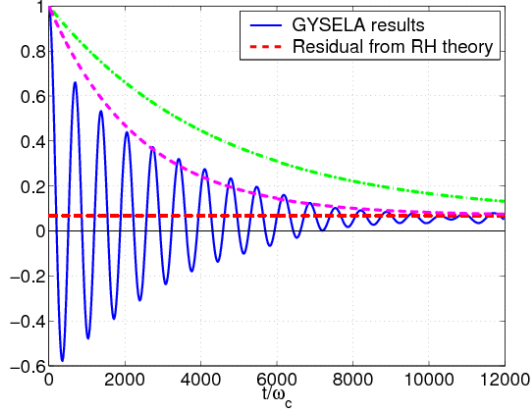


**FIGURE 5.** Time evolution of the zonal flow potential obtained by GYSELA code (solid line) and comparison with the dotted horizontal line representing the analytical residual given by Rosenbluth-Hinton theory  $A_R = 1/(1 + 1.6q^2/\sqrt{\epsilon})$ . Comparison with theoretical damping rate of the GAM. Plot of  $\hat{\phi}_{00}(t)/\hat{\phi}_{00}(t = t_0) = (1 - A_R)\exp(-\gamma_G t)\cos(\gamma_G t) + A_R$  in dashdot line for the classical values of  $\gamma_G$  and  $\omega_G$  given by [14] and in dotted line for the values given by [17] taking into account the Finite-Orbit-Width effects.

the collisionless damping is considered to affect a saturation amplitude of the ITG turbulence. These important observations have led to another classical testbed of toroidal gyrokinetic simulations [13, 14, 6, 15]. This test predicts the residual flow level in response to an initial flow perturbation governed by the radial shape of the  $(0,0)$  mode of the electric potential  $\hat{\phi}_{00}(t_0)(r)$  [16]. This initial state leads to the development of Geodesic Acoustic Modes (GAMs) which are  $(m,n) = (0,0)$  modes coupled to sidebands  $(m,n) = (\pm 1,0)$  due to the toroidal geometry. These GAMs are Landau-damped because of the finite poloidal wavenumber of the sideband. However there also exist an undamped component  $(m,n) = (0,0)$  which corresponds to the ZF. This residual value of ZF has been analytically predicted [16] by:  $\hat{\phi}_{00}(t_\infty) = \frac{\hat{\phi}_{00}(t_0)}{1 + 1.6q^2/\sqrt{\epsilon}}$ . As seen on the figure 5 the residual zonal flow level obtained by GYSELA agrees with the Rosenbluth-Hinton theory. This simulation has been performed with a safety factor profile  $q(r)$  equal to  $1.5 + 1.5(r/a)^{1.9}$  which corresponds to  $q(r_p) = 1.9$ . The frequency and the damping rate of the GAMs are also theoretically predicted [14] with:  $\omega_G = (\frac{7}{4} + \tau)^{1/2} \frac{v_{Ti}}{R}$  and  $\gamma_G = \omega_G \exp(-q^2)$ . But as seen on figure 5 the behavior of the GAMs simulated by GYSELA are not in agreement with the predicted decrease of the GAMs  $\hat{\phi}_{00}(t) = \hat{\phi}_{00}(t_0)(1 - A_R)\exp(-\gamma_G t)\cos(\gamma_G t) + A_R$ . However our simulations agree with the expression of  $\omega_G$  and  $\gamma_G$  recently found by Sugama and Watanabe [17]. These expressions take into account the effects of Finite-Orbit-Width which was not the case in the previous reference expressions.

## NON-LINEAR SIMULATIONS

The following non-linear simulations have been performed with the same parameters as for the previous linear tests, except the choice of the density and temperature gradients

where the parameters are now  $\kappa_n = 2.6$ ,  $\Delta_{r_n} = 1$ ,  $\kappa_T = 12$  and  $\Delta_{r_T} = 0.8$ . The mesh grid is  $(128 \times 128 \times 32 \times 32 \times 16)$ . The time step  $\Delta t$  has been chosen equal to  $2/\omega_c$ . A global simulation of 4000 iterations, as presented in the following, requires around 37 hours of CPU time on 32 processors. The first simulation corresponds to a simulation without zonal flow, i.e. the magnetic flux surface average  $\langle \phi \rangle$  has been neglected in the Poisson equation (4). The time evolution of  $\phi^2$  presented in figure 6 (a) exhibits the two expected phases: the linear exponential increase and the non-linear saturation phase. The turbulence relaxation observed in this non-linear phase is due to the relaxation of the profiles. Indeed, the evolution of the temperature and density profiles are only fixed by the boundary conditions. There is no source to avoid the profile relaxation. This point will be improved in the future by developing a flux-driven version of GYSELA . A 3D prototype already exists and works in a satisfying manner [18]. The localization of ballooning mode structures at the low field side ( $\theta = 0$ ) is recovered, as seen on the poloidal cross-sections of  $\phi$  plotted in figures 6 (b), (c) and (d). Adding the zonal flow effects is not a trivial point. A first important point which has been already highlighted in [6, 7] is the fact that the choice of the equilibrium distribution function is crucial. Indeed, as seen on figure 7 (a), taking an equilibrium, which does not depends on the motion invariants only, leads to the development of large scale flows. The final state is dominated by these zonal flows (fig. 7 (b)) and this takeover arrives early in the simulation (at  $t = 500/\omega_c$ ). At the opposite with an appropriate choice of the equilibrium distribution function the level of ZF is considerably reduced. The simulation shows two phases: the first one with the development of ballooning mode structures (fig. 8 (b)) follows by a shearing of the convective cells (fig. 8 (c) and (d)) due to the effects of ZF.

## CONCLUSION

A new 5D global full- $f$  gyrokinetic code, named GYSELA, has been developed to study toroidal ITG driven turbulence. The particularity of this code is to use a semi-lagrangian scheme. The linear growth rates and frequencies agree with the values expected for the classical Cyclone test case. The zonal flows behave as expected in the case of the Rosenbluth-Hinton test. It is found that the decay rate and the oscillation frequency agree with expressions given recently by Sugama and Watanabe [17]. The choice of an equilibrium function which depends only on the motion invariants is crucial to prevent the onset of turbulence due to the development of large scale flows. This problem is solved by introducing a motion invariant that is close to the minor radius and by expressing the profiles as functions of this invariant.

## ACKNOWLEDGMENTS

The authors wish to thank C. Passeron for her constant help in the development of the code.

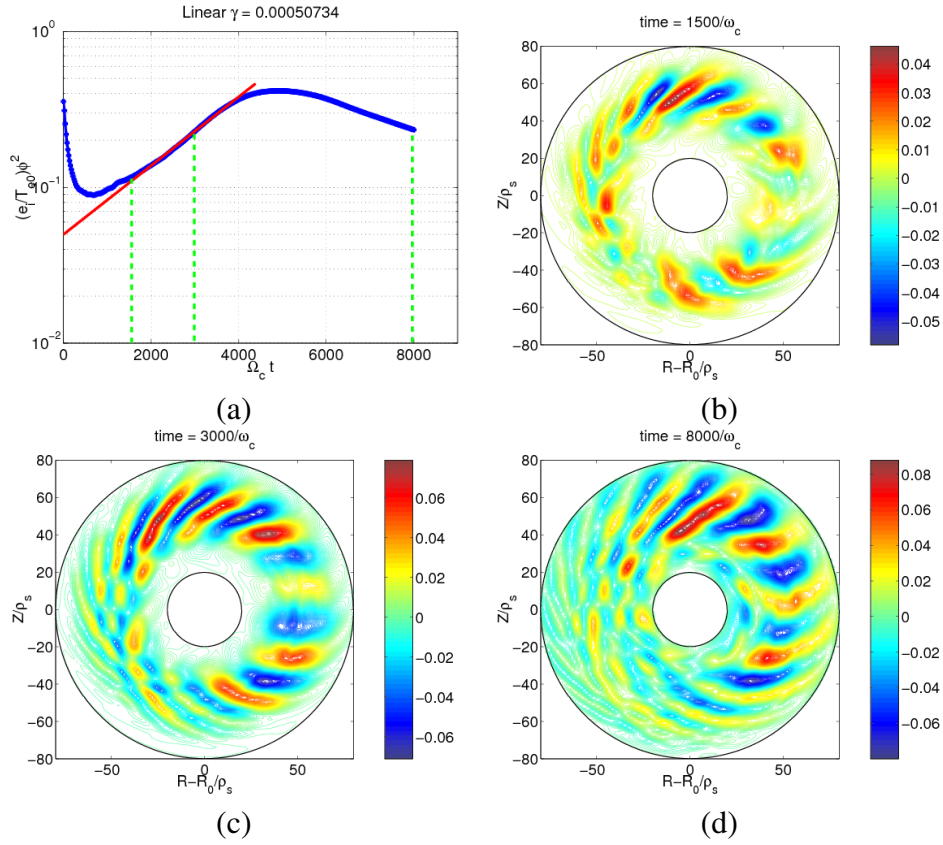


**FIGURE 6.** Time evolution of  $\phi^2$  in (a) which highlights the classical linear exponential increase and the saturation phase which begins around  $t = 4000/\omega_c$ . In this simulation the zonal flows have been artificially suppressed. The dotted vertical lines correspond to the times associated to the three poloidal cross-sections of  $\phi$  in: (b) during the linear phase ( $t = 1500/\omega_c$ ), (c) at the beginning of the saturation phase ( $t = 3000/\omega_c$ ) and (d) at the end of the simulation ( $t = 8000/\omega_c$ ).

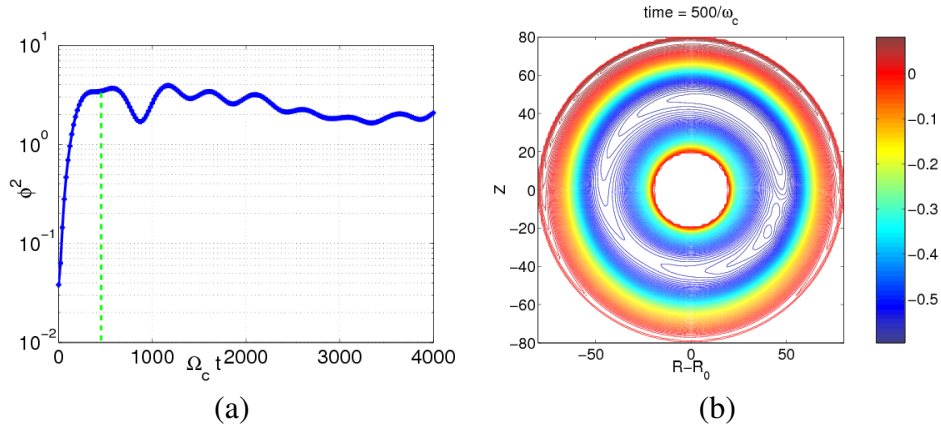


**FIGURE 7.** Simulation with zonal flows and an equilibrium part equal to the conventional Maxwellian. Time evolution of  $\phi^2$  in (a). Immediate increase of the  $(0,0)$  mode. As seen on (b) at time  $t = 500/\omega_c$ , the poloidal cross-section of  $\phi$  exhibits already a complete dominance of zonal flows.

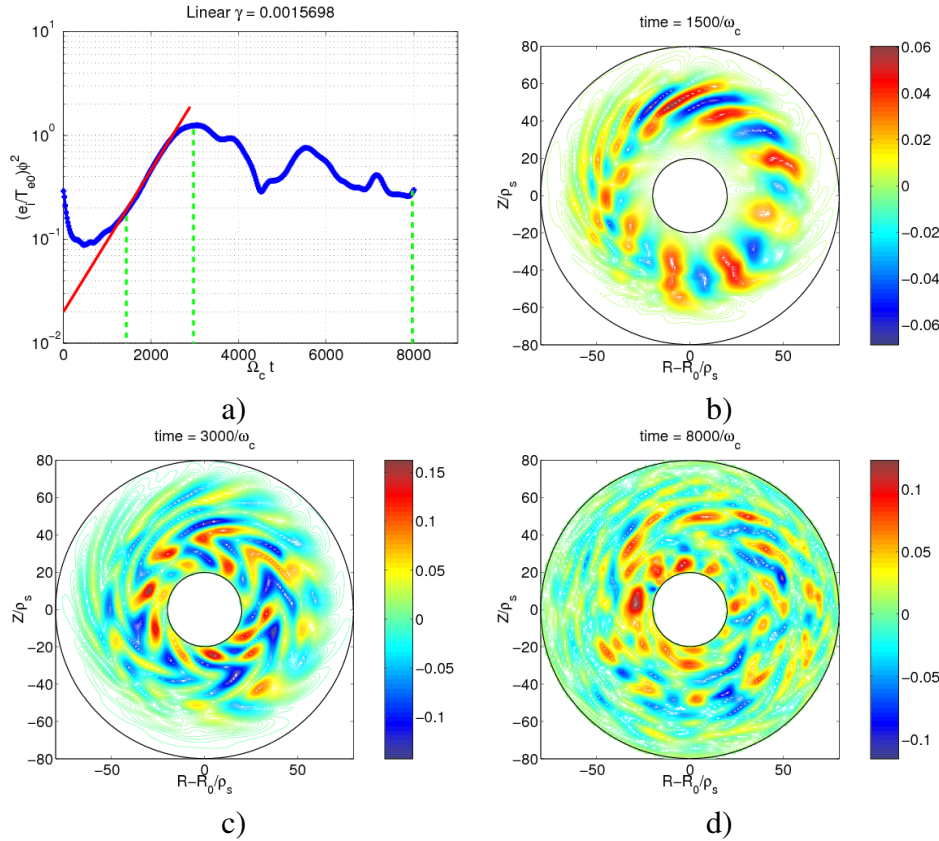


**FIGURE 8.** Simulation with zonal flows and a canonical initial distribution function. Time evolution of  $\phi^2$  in (a). Three phases exhibit with the poloidal cross-sections of  $\phi$ : (b) development of ballooning mode structure during the linear phase ( $t = 1500/\omega_c$ ), (c) and (d) shearing of the convective cells due to the effects of ZF ( $t = 3000/\omega_c$  and  $t = 8000/\omega_c$ ).

## REFERENCES

1. Nevins W. M. *et al.* Discrete particle noise in particle-in-cell simulation of plasma microturbulence. *Phys. Plasmas*, 12(122305), 2005.
2. Allfrey S. *et al.* A revised delta f algorithm for nonlinear pic simulations. *Comp. Phys. Comm.*, 154(2):898–912, 2002.
3. Sonnendrucker E. and Roche J. The semi-lagrangian method for the numerical resolution of vlasov equation. *Journal of Comput. Physics*, 149:201–220, 1999.
4. Grandgirard V. *et al.* A drift-kinetic semi-lagrangian 4d code for ion turbulence simulation. *Journal of Comput. Physics*, 217(2):395–423, 2006.
5. Sarazin Y. *et al.* Interplay between transport barriers and density gradient. *Phys. Plasmas*, 13(092307), 2006.
6. Idomura Y. *et al.* Global gyrokinetic simulation of ion temperature gradient driven turbulence in plasmas using a canonical maxwellian distribution. *Nuclear Fusion*, 43:234, 2003.
7. Angelino P. *et al.* On the definition of a kinetic equilibrium in global gyrokinetic simulations. *Physics of Plasmas*, 13:052304, 2006.
8. Dif-Pradalier G. *et al.* Defining an equilibrium state in global *full-f* gyrokinetic models. *Communications in Nonlinear Science and Numerical Simulation*, 13, 2008 (on-line July 2007).
9. Strang G. On the construction and comparison of difference schemes. *SIAM J. Numer. Anal.*, 5:506–517, 1968.

10. DeBoor C. A practical guide to splines. *Applied Mathematical Sciences* 27, 2001.
11. Dimits A. M. *et al.* Comparisons and physics basis of tokamak transport models and turbulence simulations. *Physics of Plasmas*, 7(3):969–983, 2000.
12. Rosenbluth M.N. and Hinton F.L. Poloidal flow driven by ion-temperature-gradient turbulence in tokamaks. *Phys. Rev. Letters*, 80(4), 1998.
13. Lin Z. *et al.* Gyrokinetic simulations in general geometry and applications to collisional damping of zonal flows. *Phys. Plasmas*, 7(5):1857–1862, 2000.
14. Candy J. and Waltz R.E. An eulerian gyrokinetic-maxwell solver. *Journal of Comput. Physics*, 186(2):545–581, 2003.
15. Watanabe T.H. and Sugama H. Velocity-space structures of distribution function in toroidal ion temperature gradient turbulence. *Nuclear Fusion*, 46:24–32, 2006.
16. Hinton F.L. and Rosenbluth M.N. Dynamics of axisymmetric  $e \times b$  and poloidal flows in tokamaks. *Plasma Phys. Control Fusion*, 41, 1999.
17. Sugama H. and Watanabe T.H. Collisionless damping of zonal flows in helical systems. *Phys. Plasmas*, 13(012501), 2006.
18. Darmet G. *et al.* Intermittency in flux driven kinetic simulations of trapped ion turbulence. *Communications in Nonlinear Science and Numerical Simulation*, 13, 2008 (on-line July 2007).